



# Cr-rich structure evolution and enhanced mechanical properties of CoCrFeNi high entropy alloys by mechanical alloying

Artur Olejarz<sup>a,\*</sup>, Wenyi Huo<sup>a,b,\*\*</sup>, Damian Kalita<sup>a</sup>, Maciej Zieliński<sup>a</sup>, Edyta Wyszowska<sup>a</sup>, Witold Chromiński<sup>a,c</sup>, Ryszard Diduszko<sup>a</sup>, Marcin Chmielewski<sup>a,d</sup>, Iwona Jóźwik<sup>a</sup>, Łukasz Kurpaska<sup>a</sup>

<sup>a</sup> NOMATEN Centre of Excellence, National Centre for Nuclear Research, A. Sołtana 7, 05-400, Otwock, Świerk, Poland

<sup>b</sup> College of Mechanical and Electrical Engineering, Nanjing Forestry University, Nanjing, 210037, China

<sup>c</sup> Faculty of Materials Science and Engineering, Warsaw University of Technology, Woloska 141, 02-507, Warsaw, Poland

<sup>d</sup> Lukasiewicz Research Network, Institute of Microelectronics and Photonics, 32/46 Al. Lotników, Warsaw, 02-668, Poland

## ARTICLE INFO

### Keywords:

High entropy alloys  
Mechanical alloying  
SEM  
X-ray diffraction  
Nanoindentation  
Chromium carbides

## ABSTRACT

Mechanically-alloyed CoCrFeNi high entropy alloys (MA-HEAs) show better mechanical properties than as-cast HEAs. However, the limited amount of powder milled in one-milling cycle creates a challenge in larger-scale applications. The low ball-to-powder ratio (BPR) milling used to increase powder yield resulted in the formation of Cr-rich second phases in the face-centered cubic matrix. To overcome the above issues, in this work, with a low BPR of 5:1, four different processes were analyzed: quicker milling intervals, higher milling speed, and the pre-alloying of Cr and Ni. All parameters mentioned before were used and tested together in the fourth sample. Samples were consolidated by spark plasma sintering technique. Microstructural characterization was made on a Scanning Electron Microscope equipped with EDS and EBSD detectors and a Transmission Electron Microscope. X-ray diffraction was employed to develop the structural evolution of powders sintered and annealed samples. The global hardness was measured using microhardness tests, while the nanohardness tests helped us correlate the evolution of secondary phases with their mechanical properties. The results show that pre-alloying elements with the lowest diffusion coefficient before the main milling process might be an attractive strategy to improve productivity and optimize microstructure without limiting the efficiency of low BPR MA-HEAs. The results described below demonstrate the promising perspective for the implementation of powder metallurgy techniques in a mass scale production as low BPR is essential for numerous applications like aerospace industry, car engines and medicine, where improved productivity of powder mixing is mandatory.

## 1. Introduction

Powder metallurgy (PM) could be a suitable alternative for many applications. The primary objective of all powder metallurgy methods is to mix all the desirable elements in powder form in a proper composition and perform consolidation to obtain the bulk material [1]. This group of methods was first adapted to the ceramics-reinforced steel [2]. Incorporation of other refractory phases is difficult or practically impossible using traditional techniques. Powder metallurgy techniques have been developed and adapted in many ODS- or carbide-reinforced systems [3–7].

Powder metallurgy is a broad term; therefore, two different processes

might be distinguished. Among many techniques described in the literature, mechanical alloying (MA) is predominantly used for powder production [8,9]. Powder particles with the selected chemical composition are milled in the jar [1,8,9]. Mechanical alloying allows the operator to control the process by tuning many parameters despite the process being time-consuming. The process optimization results in enhanced properties of synthesized entities, i.e., higher densification or improved homogenization. Consequently, these factors lead to augmented functional properties of the synthesized objects [10–12]. Spark Plasma Sintering (SPS) is a commonly used technique for powder compaction [1,7,13–16]. The prominent advantage of this method is implementing the external heating source, which is introduced to the

\* Corresponding author.

\*\* Corresponding author. NOMATEN Centre of Excellence, National Centre for Nuclear Research, A. Sołtana 7, 05-400, Otwock, Świerk, Poland.

E-mail addresses: [artur.olejarz@ncbj.gov.pl](mailto:artur.olejarz@ncbj.gov.pl) (A. Olejarz), [wenyi.huo@ncbj.gov.pl](mailto:wenyi.huo@ncbj.gov.pl) (W. Huo).

<https://doi.org/10.1016/j.jmrt.2024.03.116>

Received 20 November 2023; Received in revised form 27 February 2024; Accepted 19 March 2024

Available online 22 March 2024

2238-7854/© 2024 The Authors. Published by Elsevier B.V. This is an open access article under the CC BY-NC license (<http://creativecommons.org/licenses/by-nc/4.0/>).

powder particles via a graphite die by direct current [17,18]. This mechanism guarantees that the material's formation occurs significantly below the melting points of its constituents. Thus, the technique enables producing compositions that have not been developed nor analyzed before [19].

The fields of PM applications are undergoing continuous expansion. One of these fields is manufacturing high entropy alloys [11–13]. The idea of HEA is to mix a few elements with no dominant one and form a single (or dual) phase structure [1,8]. The chemical composition of the alloy must be chosen very carefully to avoid unexpected intermetallic formation [8,17,20]. The above factors might be critical for adapting powder metallurgy to manufacturing high-entropy alloys. Finely subdivided powder particles enable a close match of the powder precursors' composition ratio. On the other hand, the rapid sintering process hinders unexpected phase formation or element segregation. Besides, powder metallurgy provides an opportunity to introduce reinforcement phases (e.g. ceramics) to improve some properties significantly. This forces the PM to be placed next to 3-D printing methods as the most promising for manufacturing HEA on a mass scale.

As mentioned, many parameters might be set up during the milling and sintering processes to promote expected properties. For this reason, the manufacturing process using powder metallurgy techniques must be optimized with respect to the inherent characteristics of each alloying powder. Numerous investigations concerning the milling time have been performed, revealing the progressive structural changes occurring within the milled powders [11,21]. However, it is worth noting that prolonged milling time may lead to difficulties in crystal structure analysis due to large diffraction peaks broadening originating both from small crystallite size and increased density of defects leading to local strains of the crystal lattice, or undesired phase formation [1]. Moreover, milling breaks must be employed to prevent overheating of the milling system [22,23]. Salemi et al. revealed that the milling of CuNi-CoZnAl at the speed of 300 rpm is insufficient for FCC-phase formation even after 50 h [24]. However, increasing the milling speed to 350 rpm with balls of different radii leads to the fully synthesized powder. One should remember that even the size of powder precursors or the differences in the diffusion rates of elements may impact the product's final quality. Suprianto et al. implied that pre-milling Cr and Ni before the main milling promotes a more refined microstructure and uniform distribution of oxides formed in-situ in Cantor alloys [25]. Nano oxides nucleate on the Ni–Cr-rich particles obtained after pre-milling. This, in turn, causes mechanical properties improvement of the product.

Beyond the efficiency aspects, the productivity of the process cannot be neglected. This might be significantly enhanced by increasing powder fraction within a single milling campaign. The easiest way to achieve this is to reduce the ball-to-powder ratio (BPR). However, this step might be risky because a low BPR harms the quality of the product [21,26]. Since the process must be adapted to a larger scale, comprehensive studies of the microstructure and functional properties of the system are necessary to find a productivity versus efficiency trade-off. Curiously, up to our knowledge, the description of low BPR impact on the synthesized sample remains unrecognized.

In this investigation, we conducted a study involving five samples of the equiatomic composition of CoCrFeNi high entropy alloys, which were subjected to different preparation methodologies, to analyze the impact of the pre-milling process, milling speeds, milling intervals, and their collective effects. All samples were produced with the same milling time and low BPR, followed by the same sintering process. A sample prepared by a typical manufacturing process with a higher BPR was used as a reference. In this study, optical microscopy, scanning electron microscopy (SEM) equipped with Energy-Dispersive X-ray Spectroscopy (EDS) and Electron Backscatter Diffraction (EBSD) detectors, transmission electron microscopy (TEM), and X-ray diffraction (XRD) techniques were employed to analyze the structural evolution of the materials. Microhardness and nanoindentation tests assessed the mechanical properties at two different scales. This study endeavors to

elucidate the inquiries surrounding the potential impact of modifications in the manufacturing process on the resulting carbide formation and mechanical properties of materials. The second aim is a comparative analysis of the efficiency of the process, contrasting the current methodology with a similar process wherein a higher BPR has been implemented.

## 2. Experimental

### 2.1. Sample preparation

In this work, Co (<1.6  $\mu\text{m}$ , purity: 99.8%), Cr (<45  $\mu\text{m}$ , purity: 99.0%), Fe (<10  $\mu\text{m}$ , purity 99.9%), and Ni (<37  $\mu\text{m}$ , purity: 99.8%) powders produced by Alfa Aesar were mixed in equiatomic composition under an Ar atmosphere and placed in a tungsten carbide (WC) jar with WC balls. Powders were milled in the Retsch PM100 high-energy ball milling system. A ball-to-powder ratio of 5:1 and a cumulative milling time of 40 h in the main milling process were used for all samples. N-heptane was added to avoid cold welding. The impact of different parameters on the final products was tested. For the first sample, named PA, the pre-alloying process with BPR 10:1 for 10 h and a milling speed of 350 rpm was employed for Cr and Ni powders before the main milling started. A short pre-alloying process was performed on milled powders with the lowest diffusion rate and largest particle size (below 45  $\mu\text{m}$  and 37  $\mu\text{m}$ , respectively). The main milling process was performed with a milling speed of 250 rpm. The mixing process was conducted in 15-min intervals (15 min of milling and 15 min of breaks). Different intervals were used for the second sample, and only 5-min pause after 15 min of milling was applied. Shorter milling breaks were utilized to see if that short time is still enough to avoid cold welding of powder particles. The milling speed of 250 rpm was kept, and the sample was labeled MI. The milling speed for the third sample labeled MS was increased to 350 rpm, and equal milling intervals were restored. In both MI and MS samples, the pre-milling process was not implemented. All the factors described above were analyzed simultaneously in the fourth sample noted as MIX: milling speed: 350 rpm, 5-min breaks after 15 min of milling and short pre-alloying process following the same procedure as in PA samples. Moreover, a sample with identical chemical composition was prepared by a typical manufacturing process [1,27]. The BPR was 10:1, the milling speed was 250 rpm, and intervals of 15:5 min were employed during 40 h of the milling process and noted as BM. The samples' names with all applied process parameters were collected in Table 1.

After mechanical alloying, the consolidation process was carried out using the spark plasma sintering technique. The process was performed in a moderate vacuum ( $10^{-2}$  mbar). A constant pressure of (50 MPa) and a temperature of 950  $^{\circ}\text{C}$  was maintained during the sintering. The holding time was 10 min at a target temperature. After sintering, the samples were mechanically ground to remove a graphite layer formed as the result of the usage a graphite die during synthesis. The heat treatment performed at 1050  $^{\circ}\text{C}$  for 12 h in quartz tubes under Argon atmosphere to homogenize the materials was followed by water quenching. Moreover, PA and MIX, as samples milled in two steps, were selected to be annealed at two different temperatures: 850  $^{\circ}\text{C}$  and 1050  $^{\circ}\text{C}$  for 12 h. The decision of two different temperatures employment for these two samples was motivated by different secondary phases' evolution path compared to the samples milled in one milling cycle.

After the sintering and annealing, the samples were ground with

**Table 1**  
Characteristic process parameters of the investigated specimens.

	PA	MS	MI	MIX
Characteristic parameter:	Extra pre-alloying	Milling speed	Milling intervals	All parameters
Value	10 h	350 rpm	15:5 min	All three together

sandpapers: #320 to #2500 and then electropolished using a mixture of 8% perchloric acid with 92 % ethanol. The electropolishing process was performed under 25 V for 20 s at 0 °C.

## 2.2. X-ray diffraction

Diffraction patterns (DPs) acquisition was performed using a divergent X-ray beam and the Bragg-Brentano parafocusing geometry at the Bruker D8 Advance diffractometer with a  $\theta/\theta$  goniometer of a 280 mm radius and Cu K $\alpha$  radiation ( $\lambda = 1.54 \text{ \AA}$ ). Data were collected in the  $2\theta$  range from  $20^\circ$  to  $145^\circ$  at room temperature by a LYNXEYE XE-T detector working in high-resolution 1D mode without a Ni-filter and with a window covering  $2.941^\circ$  of  $2\theta$ . The primary optics was optimized to the available sample surface by setting the right size of the fixed divergence slit and the beam vertical mask accounting for beam spill limited by  $2.5^\circ$  axial Soller slits. The detector optics contained only  $2.5^\circ$  axial Soller slits. Additional diffraction pattern was collected in the  $2\theta = 30^\circ \div 67^\circ$  range for each specimen in order to ease the analysis of the minor carbide and oxide phase, in which weak peaks were spotted in this scattering region.

The Bruker DIFFRAC.EVA program with the database of diffraction standards ICDD PDF4+ 2022 [28] and DIFFRAC.TOPAS programs were used for phase analysis and to refine the models of the identified phases to satisfactorily describe the experimental diffraction patterns. The TOPAS program uses the fundamental parameters profile fitting (FPPF) approach to account for instrumental effects and Rietveld approach [29, 30] to optimize the model crystal structures' parameters.

The contribution of the specimen to the diffraction peak shape shall be considered in terms of its origin from crystal domains sizes and local strains of the crystal lattice caused by point and line defects (a strain shall be interpreted as a deviation from a reference, e.g. average, distance e.g. among crystal planes –  $\Delta d/d$ , where  $d$  is the interplanar distance). Following e.g. D. Balzar [31], these contributions can be separated from each other judging by the evolution of the full width at half maximum (FWHM) of the consecutive peaks with the  $2\theta$  angle and by the peak shape being described by the Voigt function with greater Gaussian or Lorentzian share. In the absence of size-broadening, i.e. when the crystal domains that scatter coherently are bigger than at least 200 nm (which holds in our case for the sintered and annealed samples), the remaining lattice strain-related broadening shall make the FWHMs to scale as  $\tan \theta$ .

Deviations from  $\text{FWHM} \sim \tan \theta$  indicate that the lattice strains ( $\epsilon$ ) differ along different crystallographic directions, due to the varying density and/or type of defects, i.e. anisotropy of strains is present. A phenomenological model by P. W. Stephens [32] accounts for this by introducing, for a cubic phase, 3 additional parameters:  $\eta$ ,  $S_{400}$  and  $S_{220}$ , which correlate the FWHM deviations with  $(hkl)$  planes spacing and  $hkl$  peaks' indices. Following A. Leineweber [33], these parameters are related to the variance of strain,  $\langle(\Delta\epsilon_{hkl})^2\rangle$ , in different crystallographic directions, normal to  $(hkl)$  planes.

Correct models describing the experimental diffraction patterns were necessary to establish the FCC phases lattice constant values, although it was the crystal phases composition, rather than the phases' crystal structures, which investigation was the primary objective of our research.

## 2.3. Microstructural studies

ThermoFisher Helios 5 UX scanning electron microscope was employed to study the microstructural evolution of sintered and annealed samples. The microscope was equipped with the EDAX Octane Elite Plus EDS system and EDAX Velocity Pro electron EBSD camera. The microstructural observations were performed in the backscattered electrons (BSE) channeling contrast. EBSD mapping was carried out with a step size of 0.1  $\mu\text{m}$ . The obtained data were analyzed using the EDAX OIM Analysis 8 software. Points with a confidence index (CI) below 0.1

were excluded from the calculations.

The transmission electron microscopy studies were performed using the JEOL JEM 1200EX II (operating at 120 kV) and JEOL JEM F200 (operating at 200 kV). The samples for TEM analysis were prepared using the lift-out focused ion beam (FIB) technique. The final thinning of the samples was performed at 2 keV beam energy to reduce the density of defects introduced by the  $\text{Ga}^+$  ions.

## 2.4. Hardness measurements

The hardness of the specimens was measured using a Zwick Dura-Vision macro hardness tester with a Vickers type indenter by applying a 1 kg load and 15 s dwell time. At least six measurements on each sample were carried out. Nanoindentation was performed using a NanoTest Vantage system from Micro Materials. A Synton-MDP diamond Berkovich-shaped indenter was used in this study. Tests were conducted using a 50 mN load. Thirty-six indentations were performed on each sample with 30  $\mu\text{m}$  spacing between the indents. The Fisher-Cripps relation was used to calculate the relationship between Vickers microhardness HV and Berkovich nanohardness HB, which was done by employing Eq (1):

$$H_V \left[ \frac{\text{kg}}{\text{mm}^2} \right] = 94.495 H_B$$

## 3. Results

### 3.1. Density

Density measurements were performed using the Archimedes method on a RADWAG X2 series. At least five measurements were carried out on each sintered and annealed sample. The results were presented in Table 2. The theoretical density was estimated based on Eq. (2):

$$\rho = \frac{4m_{\text{aAvg}}}{V_{\text{cell}}},$$

where  $m_{\text{aAvg}}$  corresponds to the averaged atomic mass of Co, Cr, Fe, and Ni, and  $V_{\text{cell}}$  is the volume of an FCC unit cell calculated with the lattice constants derived from XRD data [34]. The volumes of the real FCC cells calculated by XRD reaches  $3.5708 \pm 0.0002 \text{ \AA}$ . Due to the very small discrepancies the theoretical density was calculated from the average lattice parameter. The average theoretical density is means in turn the average mass of a unit cell (4 atoms in each) divided by theoretical density and for all samples was estimated as  $8.23 \text{ g/cm}^3$

The obtained materials present a high densification level. All the results exceed 95% of the theoretical density. This observation confirms the high quality of the sintered samples. The heat treatment process further improved the densification of materials. The density of annealed MIX and MI samples reached 97% of the theoretical density. Moreover, the obtained data are similar to those previously reported in the literature [4,35]. Both facts lead us to believe that the number of pores in the specimens is negligible.

**Table 2**

Measured density of the specimens before and after annealing.

Density [ $\text{g/cm}^3$ ]	BM	MS	MI	PA	MIX
Before annealing	$7.91 \pm 0.07$	$7.91 \pm 0.05$	$7.91 \pm 0.06$	$7.86 \pm 0.07$	$7.83 \pm 0.04$
After annealing at 850 °C	–	–	–	$7.98 \pm 0.05$	$7.90 \pm 0.04$
After annealing at 1050 °C	$7.89 \pm 0.07$	$7.85 \pm 0.06$	$8.01 \pm 0.10$	$7.91 \pm 0.04$	$8.01 \pm 0.05$

### 3.2. X-ray diffraction

Fig. 1 (a) shows the PXRD patterns of the as-milled powders after 40 h of milling and the Cr–Ni powder pre-milled for 10 h. In all samples, two other types of crystal phases dominate the DPs, namely FCCs and BCCs. In fact, peaks of both crystal phases consist of a few peaks, which was demonstrated in detail in Fig. 1 (b). Apart from the MIX sample, in diffraction patterns (DPs) of all others, i.e., BM, MS, MI, and PA, diffraction peaks of pure elements can still be observed, especially the ones originating from the Co HCP phase (see Fig. 1(b)). Such a case points to the low efficiency of the main milling process.

Judging by the shapes of FCC and BCC diffraction peaks, that exhibit multiple maxima and/or long shoulders usually extending toward lower  $2\theta$  angles (the lower the position of the peaks, the higher the lattice parameter,  $a_{\text{Ni}}$  seems to be the bottom limit), it is clear that mechanical alloying results in formation of such phases with varying compositions and defects density. Further evidence is provided by the intensities of sequential peaks that differ from the values predicted by the structure factors of typical FCC and BCC phases and by the shift of selected peaks of FCC phases, e.g., 200, from their position predicted by fitting a model structure to other peaks of a given phase. The former observation, concerning the intensity, suggests at least one of the following effects to occur: the varying occupation of sites by atoms of different elements; possible presence of interstitial atoms or vacancies; and some degree of disorder (namely, deviations of the particular atom position from its lattice node). The latter phenomenon, the selected peak shift, can be interpreted as a higher density of stacking faults, according to B. E. Warren [36].

The BCC phase peaks, if observed in the DP, are always positioned close to either Fe or Cr typical positions. This is the case also for the 10h pre-milled sample. Hence, it seems that the mechanism of alloying is based on migration and diffusion of Fe and Cr atoms into the FCC phases, which, of course, mix together as well.

The DPs of sintered samples are presented in Fig. 2 (a). They all can be fitted by one FCC phase model accompanied by secondary phases:  $M_{23}C_6$ ,  $M_7C_3$ , and  $M_2O_3$ , where M means a metal, but no evidence for pure elements can be found anymore. “M” should be mostly associated with Cr, but solid solutions with other elements cannot be dismissed. We will use the name chromium carbides for simplicity and following the electron microscopy results. Their crystal structure investigation is rough only (applies also to estimates of concentration) due to very few peaks of low intensity observed in DPs.

The FCC phases in sintered samples always require the Stephens model accounting for crystal lattice strain anisotropy and deviations from the average value in different crystallographic directions because

FWHMs of consecutive peaks do not smoothly follow the  $\tan(2\theta)$  correlation. The lattice parameter of the FCC matrices in all samples is, on average,  $3.5708 \pm 0.0002 \text{ \AA}$ , as widely reported before [4,37,38].

Depending on the chosen milling process, one or two metallic carbides were formed (see Table 3) after SPS.  $Cr_{23}C_6$  is present in all sintered samples and is marked by black stars in Fig. 2(b–d). The total content of  $Cr_{23}C_6$  ranges between 6.0 and 9.0 wt%. This narrow range indicates no impact of the evolution of one milling parameter on the content of  $Cr_{23}C_6$ . Chromium oxide ( $Cr_2O_3$ ) is detected in all samples, too, and marked by white circles in Fig. 2(b–d). The correlation between the content of  $Cr_{23}O_6$  or  $Cr_2O_3$  and the milling process was not observed. The average oxide concentration is  $2.0 \pm 0.6 \text{ wt\%}$ . In the MIX sample, additionally, a  $Cr_7C_3$  phase is observed marked as “X”, see Fig. 2 (c) and Table 3.

Fig. 3 (a) shows the XRD patterns of annealed samples. In general, the content of the FCC phases increased in all annealed samples at the expense of chromium carbides compared to their state before the thermal treatment. Only in the MIX 850 °C sample  $Cr_7C_3$  converted to  $Cr_{23}C_6$ , which also yielded an increase of carbides content from 10.3 wt% to 12.8 wt%. These observations suggest the structural evolution of annealed samples. Moreover, depending on manufacturing process parameters, the direction of the evolution is different. The MS and MI samples present a similar amount of  $Cr_{23}C_6$  marked as the black star in Fig. 3 (f). Notably, despite the similar composition of sintered samples, the as-annealed BM patterns show two carbide structures in close proportion, which is listed in Table 3. Similarly, in PA, after annealing at 1050 °C the formation of  $Cr_7C_3$  is promoted, as can be seen by ‘X’ in Fig. 3 (e). Still, after annealing at 850 °C, only the peaks of  $Cr_{23}C_6$  were observed (see black star in Fig. 3 (d)). Combining all special parameters in the MIX sample results in one type of carbide formation at both temperatures. However, at 850 °C, peaks of  $Cr_{23}C_6$  were detected, which is demonstrated in Fig. 3 (b), while at higher temperatures,  $Cr_7C_3$  was found in Fig. 3 (c). The cumulative content of carbides for the MS, MI, BM, and PA samples is similar (3.3–6.3 %), while the MIX samples present a higher content of carbides, as the sintered MIX sample did. The amount of chromium oxides in all samples remained at the same level (1.4–2.7 %), so the impact of the annealing process on the amount of  $Cr_2O_3$  was not found. The contents of minor phases in all samples after sintering and annealing are collected in Table 3.

### 3.3. Microstructural studies

The SEM images of the sintered samples are presented in Fig. 4. The grain sizes range from several to tenths of microns for all the studied samples. Moreover, different secondary phases were formed depending

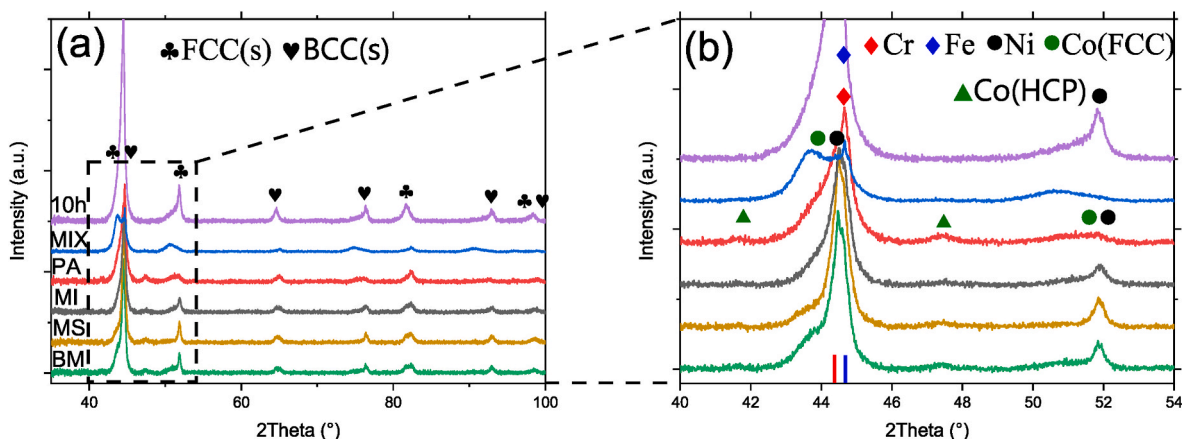


Fig. 1. (a) XRD patterns of powders in the  $2\theta$  range from  $35^\circ$  to  $100^\circ$  with (b) magnification of the  $2\theta$  range  $40^\circ$ – $54^\circ$ . Red and blue lines means typical Cr and Fe peaks according to PDF cards number: 00-006-0694 (bcc-Cr) and 00-006-0696 (bcc-Fe). (For interpretation of the references to colour in this figure legend, the reader is referred to the Web version of this article.)

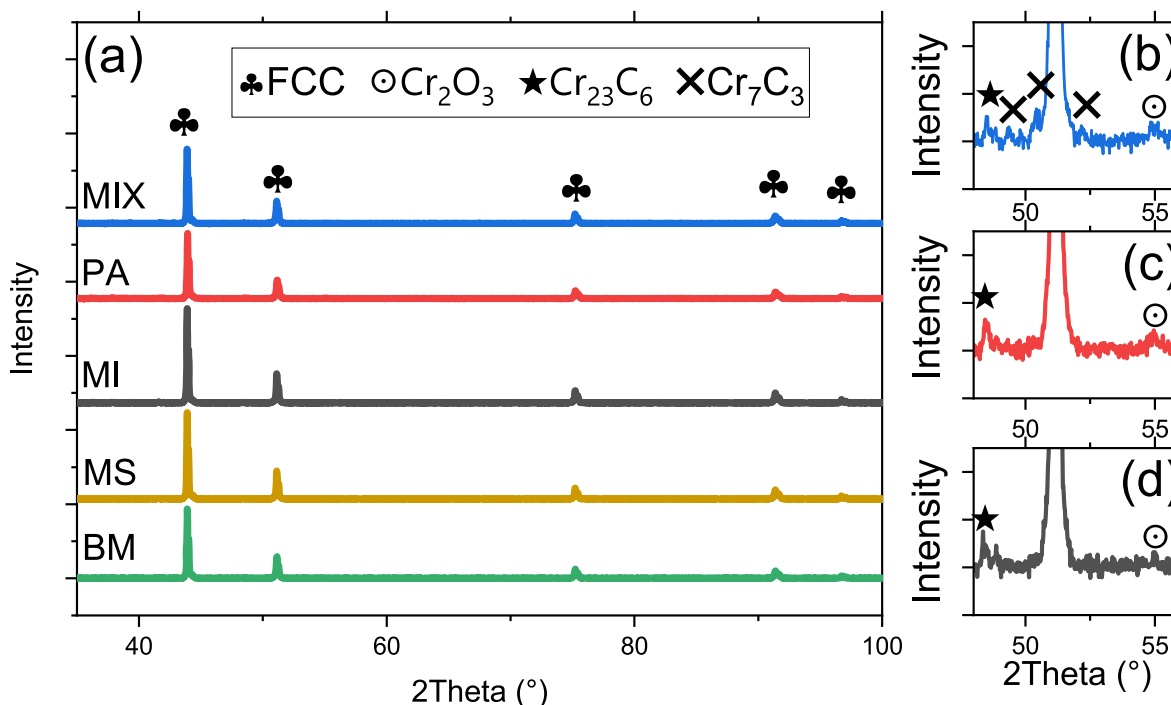


Fig. 2. (a) XRD patterns of sintered samples; highlighted 47–55.5° regions of (b) MIX, (c) PA, (d) MI sintered samples.

**Table 3**  
Carbides content in different samples.

Sample	Process	Cr <sub>23</sub> C <sub>6</sub>	Cr <sub>7</sub> C <sub>3</sub>
BM	Sintered	8.8 %	–
	Annealed 1050 °C	3.1 %	3.2 %
MS	Sintered	8.8 %	–
	Annealed 1050 °C	4.7 %	–
MI	Sintered	6.5 %	–
	Annealed 1050 °C	3.9 %	–
PA	Sintered	7.8 %	–
	Annealed 850 °C	5.8 %	–
	Annealed 1050 °C	1.1 %	2.2 %
MIX	Sintered	6.0 %	4.3 %
	Annealed 850 °C	12.8 %	–
	Annealed 1050 °C	–	9.3 %

on manufacturing process parameters. For the samples milled in one-milling cycle processes, BM, MS, and MI samples (Fig. 4(a–c)), the described particles state the cohesive formations uniformly distributed throughout the volumes of the samples. Two distinct structures can be discerned within these particles: observable grains located internally, as indicated by the pink arrows in Fig. 4 (a), and an encompassing external ring pointed out by the green arrows. The EBSD maps of the typical particle will be discussed further.

The SEM-EDS technique was employed to analyze the elemental distribution of the matrix and particle (agglomerate) phases. EDS element concentration maps of MI, MS, and BM samples revealed the presence of Chromium-rich structures distributed within the matrix, marked with black arrows in Fig. 4 (c) presenting the characteristic regions of the MI sample. The Chromium content reaches 100%, while other alloyed elements might be neglected. Furthermore, small regions rich in Co, Fe, and Ni were detected in these samples.

In the PA sample, Fig. 4 (d), coarse particles are still visible however, the number of them is significantly lower compared to BM, MS and MI. The hallmark of this microstructure are evenly distributed light grey particles' clusters. The EDS maps of the PA sample demonstrated in Fig. 4 (d) confirm the presence of two distinct morphologies differing from the matrix phase, as mentioned above. A few Cr-rich particles with

outer rings may still be observed. The remaining areas of higher Chromium saturation line up with Nickel-rich areas, what is labeled by white arrows. These Cr–Ni-rich islands correspond well with clusters of small particles. Similarly, to samples MI, MS, and BM, small regions rich in other alloying elements (Fe, Co) were detected by the EDS technique.

For the MIX sample presented in Fig. 4 (e), the fine particles seem to create agglomerates that can be localized all over the sample's surface. An orange hexagon in Fig. 4 (e) marks an individual cluster of these fine particles. Detailed analysis of SEM micrographs revealed the presence of two different types of precipitates: appearing as dark grey and light grey in BSE contrast images. The results of EDS analysis of the MIX sample are shown in Fig. 4 (e). The number of particle agglomerates in the MIX sample is significantly reduced compared to PA. This conclusion has been based on the observation of significantly larger regions of the samples, which images were not included due to the manuscript's clarity (see Supplemental file Figs. S1–S2). The EDS analysis again confirms the presence of Cr–Ni-rich structures in the form of agglomerates. The decreased number of Cr–Ni-rich structures and a lack of Co-, Fe- and Ni-rich areas suggest the higher diffusion of all elements during mechanical alloying compared to PA. Moreover, small areas marked in an EDS concentration map of Cr by black circles (for the sake of clarity, only a few particles as an example) with higher Chromium content uniformly distributed in the cross-section fully correspond with the evenly distributed dark grey precipitates marked with white circles in the SEM image (Fig. 4 (e)). The lower Cr concentration areas in the EDS map reflect the distribution of light grey precipitates in the corresponding SEM image.

The results of EBSD analysis of both matrix and particle phases are illustrated in Fig. 5(a–c). The matrix phase was identified to exhibit the FCC crystal structure, while the internal zone can be indexed as the BCC crystal structure. Coupled results from EDS and EBSD analyses unambiguously suggest the presence of a pure Chromium phase inside the particles. However, the EBSD analysis did not identify the external zone (ring around the grain particle) as an FCC or BCC crystal structure. This observation suggests the emergence of a distinct third structure in this outer zone.

A similar analysis has been conducted for the samples after the

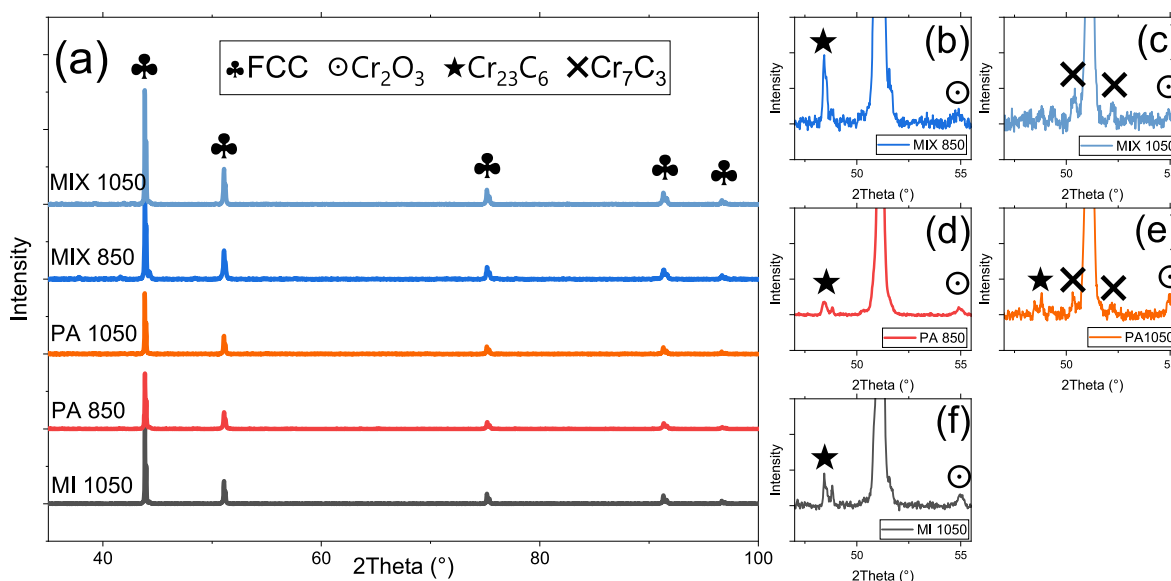


Fig. 3. (a) XRD patterns of annealed samples; (b) highlighted 47–55.5° regions.

annealing process. The EDS area analysis of the matrix phase for all annealed samples is presented in Fig. 6 (a). The plot illustrates consistent results across all samples, indicating the formation of a matrix phase with a chemical composition resembling the presumed one. A slightly lower concentration of Cr in matrix phases is related to forming secondary phases rich in Chromium (particles). The microstructure of samples after one milling cycle process is demonstrated in the MI sample in Fig. 6 (b). The microstructure consists of Cr-rich particles evenly distributed in a matrix phase. However, what is interesting is that the particles consist of only one phase, suggesting the evolution of particles at elevated temperatures.

The comparison of the microstructure of samples PA and MIX annealed at 850 °C is presented in Fig. 6 (c) and (e). These samples show similar microstructures to their counterparts before annealing, as shown in Fig. 4 (d) and (e). Agglomerates of small particles were observed, however, only one type of precipitate, called light grey, is present. The microstructure of the PA (Fig. 6 (c)) sample consists of a higher number of agglomerates (clusters). In contrast, the particles in the MIX sample are uniformly distributed in the matrix, as shown in Fig. 6 (e). Furthermore, PA presents a bimodal grain size distribution marked in yellow (coarse grains) and blue (small grains) splines in Fig. 6 (c), while the grain size distribution of the MIX sample is more uniform.

The microstructures of PA and MIX samples annealed at 1050 °C are shown in Fig. 6 (d) and (f), respectively. Heat treatment at 1050 °C caused a substantial evolution in the microstructure of both samples. The increase in the annealing temperature leads to the replacement of finely distributed particles in Cr–Ni-rich areas into agglomerates of particles in a region marked with an orange hexagon in Fig. 6 (f). The PA samples again exhibit the presence of a large number of regions of clustering particles. Furthermore, a few coarse particles known from MI, MS, and BM samples and demonstrated in Fig. 6 (a) might still be observed in PA. Moreover, dark grey particles are observed while light grey disappears when compared with Fig. 4 (e), presenting the sample before annealing.

The EDS mapping technique was again employed to understand the element distribution in the matrix and areas with a higher number of clusters of the other phases. The EDS maps of the PA sample presented in Fig. 6 (d) confirmed the uniform distribution of alloying elements in the matrix phase after the annealing process, and no Co-, Fe-, or Ni-rich areas were observed. Higher Chromium content in the particles has been detected, as in the sample before annealing.

A comparison of the average grain size of the samples annealed at

1050 °C using the EBSD technique is presented in Fig. 7 (a–c). The average grain size values for all three samples are marked in the bottom right corners of the EBSD orientation maps. Moreover, curves showing the grain size distributions are presented in Fig. 7 (d). One can see that the MIX sample exhibits the smallest and most uniform grain size. Black regions on the map correspond to the precipitates in a matrix, see Fig. 7 (c). The EBSD orientation images with the red histogram show a bimodal grain size distribution observed in PA (marked with black lines), while the samples milled in one milling cycle possess a more uniform structure, as in the MI sample, for example (Fig. 7 (a)). The regions of coarse and fine grains in the PA sample are presented in the PA-EBSD orientation image. As expected, the formation of twins in FCC materials is a common phenomenon and may be observed in all annealed samples.

The STEM bright field image of the as-sintered MIX sample is presented in Fig. 8 (a). The image shows two different particles with a size above 100 nm denoted as A and B. Two types of carbides were identified: cubic  $\text{Cr}_{23}\text{C}_6$  (selective area diffraction (SAD) in Fig. 8 (b)) and rhombohedral  $\text{Cr}_7\text{C}_3$  (SAD in Fig. 8 (c)). This observation explains well the presence of two types of particles denoted in Fig. 4 (e) and corresponds well with the X-ray diffraction pattern of the as-sintered MIX sample visible in Fig. 2 (b). The EDS maps presented in Fig. 8 (d) suggest the formation of phases rich in Chromium, which confirms the observation conducted in EDS-SEM images (Fig. 4 (e)). Moreover, significantly finer particles (below 100 nm) might be observed in bright field images. To identify this phase, the EDS technique was employed. The EDS maps presented in Fig. 8 (d) reflect the presence of chromium oxides, which were also detected by the XRD technique for all samples, as demonstrated in Fig. 2.

To denominate particles named ‘light grey’ and ‘dark grey’ (see Figs. 4 and 6), the as-annealed in 1050 °C sample was chosen. The XRD pattern and SEM image (Figs. 3 and 6) reflect only one reinforcing phase (beyond chromium oxide). The STEM bright field image of the 1050 °C MIX sample is demonstrated in Fig. 9 (a). The microstructure consists of FCC grains (SAD in Fig. 9 (b)) with other grains. The SAD analysis revealed the  $\text{Cr}_7\text{C}_3$  structure, as shown in Fig. 9 (c). This is similar as those in some recent papers [7,39]. This observation corresponds well with the previous studies, where no  $\text{Cr}_{23}\text{C}_6$  for this sample was found. The EDS analysis was again employed to reveal the presence of small chromium oxides. The EDS maps reflecting the Cr–O-rich areas are visible in Fig. 9 (d).

As previously mentioned, two types of precipitates were identified in SEM images and denoted ‘light grey’ and ‘dark grey’ precipitates. As

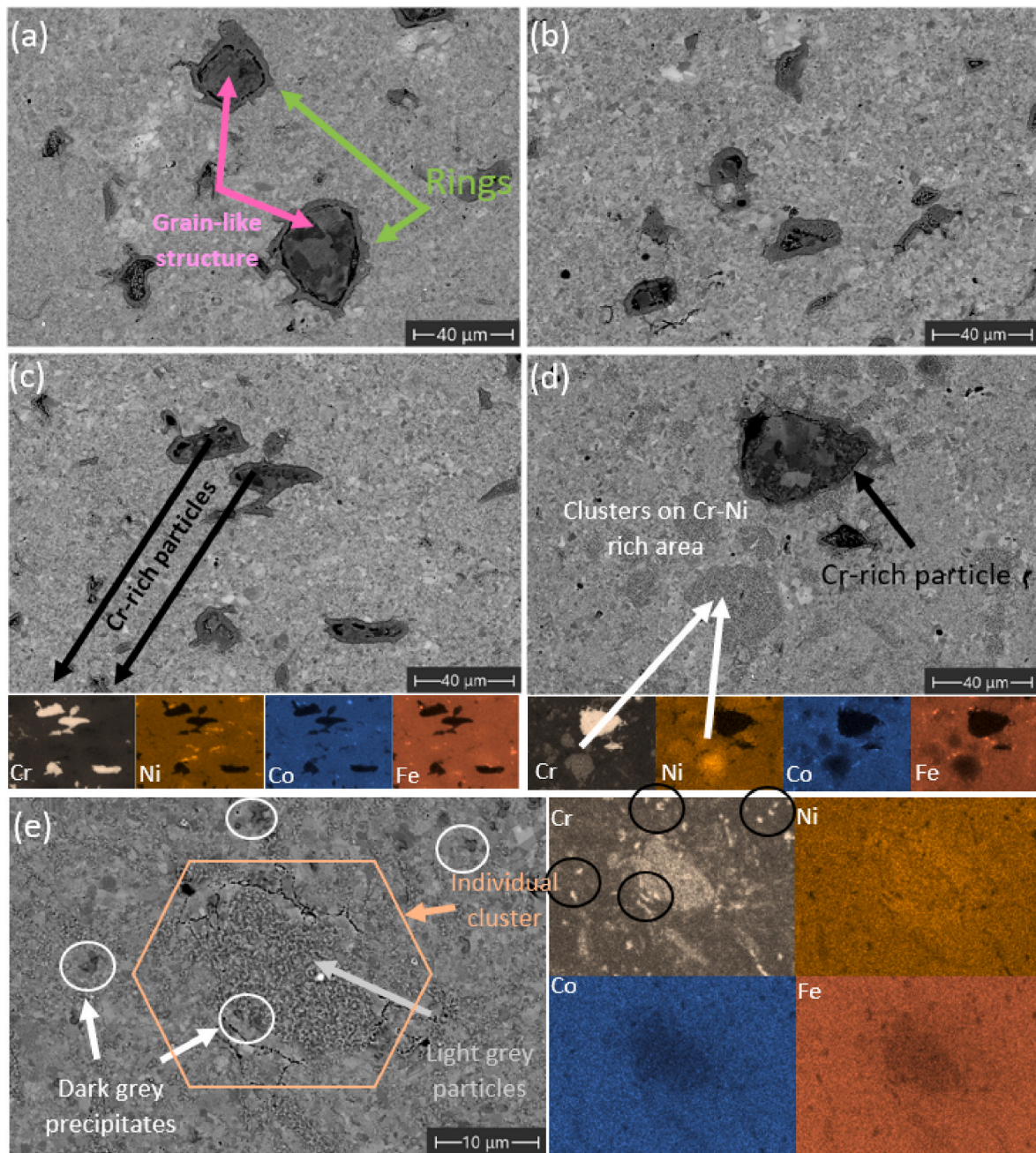


Fig. 4. Microstructure of the samples manufactured with different milling processes (a) BM sample; (b) MS sample; (c) MI sample with EDS maps; (d) PA sample with EDS maps; (e) MIX sample with EDS maps.

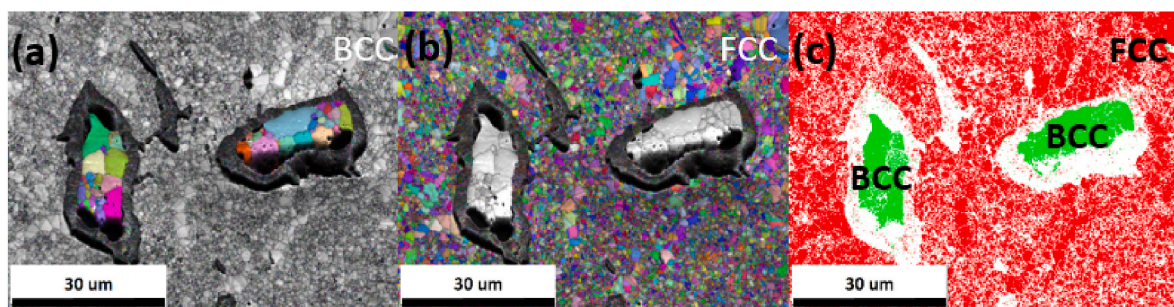
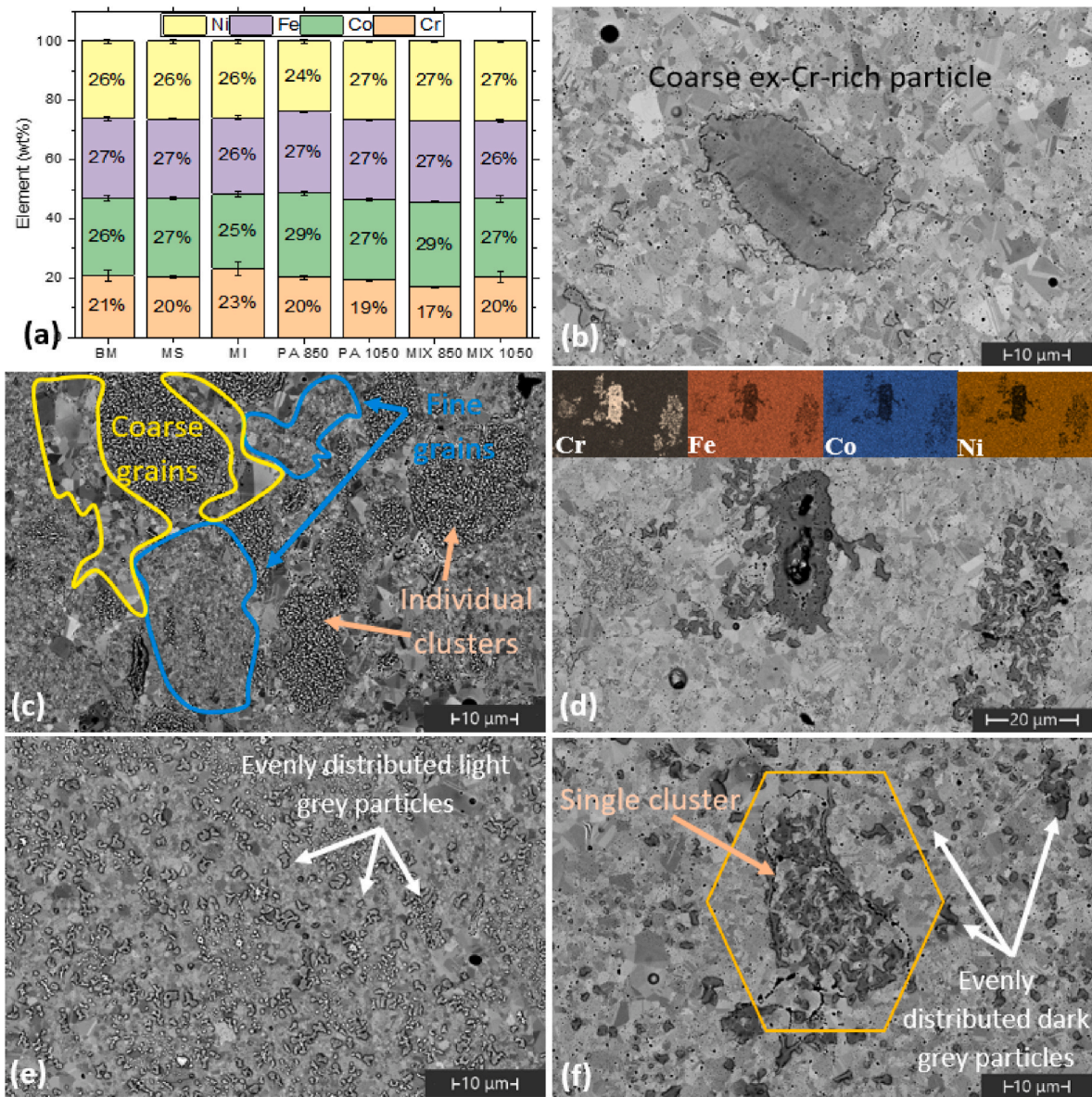


Fig. 5. EBSD orientation (a, b) and phase maps (c) of matrix and particles of the MI sample.



**Fig. 6.** EDS area analysis of annealed samples (a); microstructure of annealed samples: (b) MI; (c) 850 °C PA; (d) 1050 °C PA with EDS maps; (e) 850 °C MIX; (f) 1050 °C MIX.

shown in Fig. 8, both were identified as chromium carbides. However, the microstructure observation of the MIX sample annealed at 1050 °C (see Fig. 6 (f)) revealed only the presence of 'dark grey' particles. Both observations lead us to identify 'dark grey' precipitates as  $\text{Cr}_7\text{C}_3$  and 'light grey' as  $\text{Cr}_{23}\text{C}_6$ . Moreover, the EDS analysis confirmed the presence of much smaller  $\text{Cr}_2\text{O}_3$  particles embedded in the matrix. For the final summary, all the identified phases for all manufactured samples through the whole manufacturing processes are collected in Table 4.

### 3.4. Hardness measurements

In Table 5 the results of microhardness tests on sintered and annealed samples were collected. The evaluation using a force of 1 kgF revealed a high homogeneity of all materials at the macroscale. The average hardness of the as-sintered MIX sample exceeds 400  $\text{HV}_1$ , the highest value of all tested samples. The hardness of the as-sintered PA sample is slightly higher than that of the rest and equals 383  $\text{HV}_1$ , whereas the hardness of the others oscillates at around 360  $\text{HV}_1$ . Samples after heat treatment present reduced hardness. However, a modest drop in

hardness, below 5 %, of samples annealed at lower temperatures was detected. The specimens annealed at 1050 °C indicate that the reduction in hardness at the macroscale is approximately 23 % for all tested samples.

Fig. 10 (a) presents the representative nanoindentation curves of the as-sintered and 1050 °C as-annealed MIX samples. The maximal applied load of 50 mN results in the deformation of materials approx. 600–700 nm occurred. Considering that the plastic deformation under the indenter tip is 10x higher than the maximal indentation depth, the recorded signal represents the response of a few grains (average grains size was  $\sim 1.5 \mu\text{m}$ ) [40]. Due to the presence of different phases, only the matrix phase indents were considered. However, given that the small ( $\sim 100 \text{ nm}$ – $1000 \text{ nm}$ ) particles are evenly distributed in the sample volume, the signal reflects the weighted average nanohardness of both the matrix and precipitates. Therefore, only the agglomerates and coarse Cr-rich particles were excluded from the nanohardness results of a matrix phase.

The evolution of the nanohardness of the MI, PA, and MIX matrix phases as a function of annealing temperature is demonstrated in Fig. 10

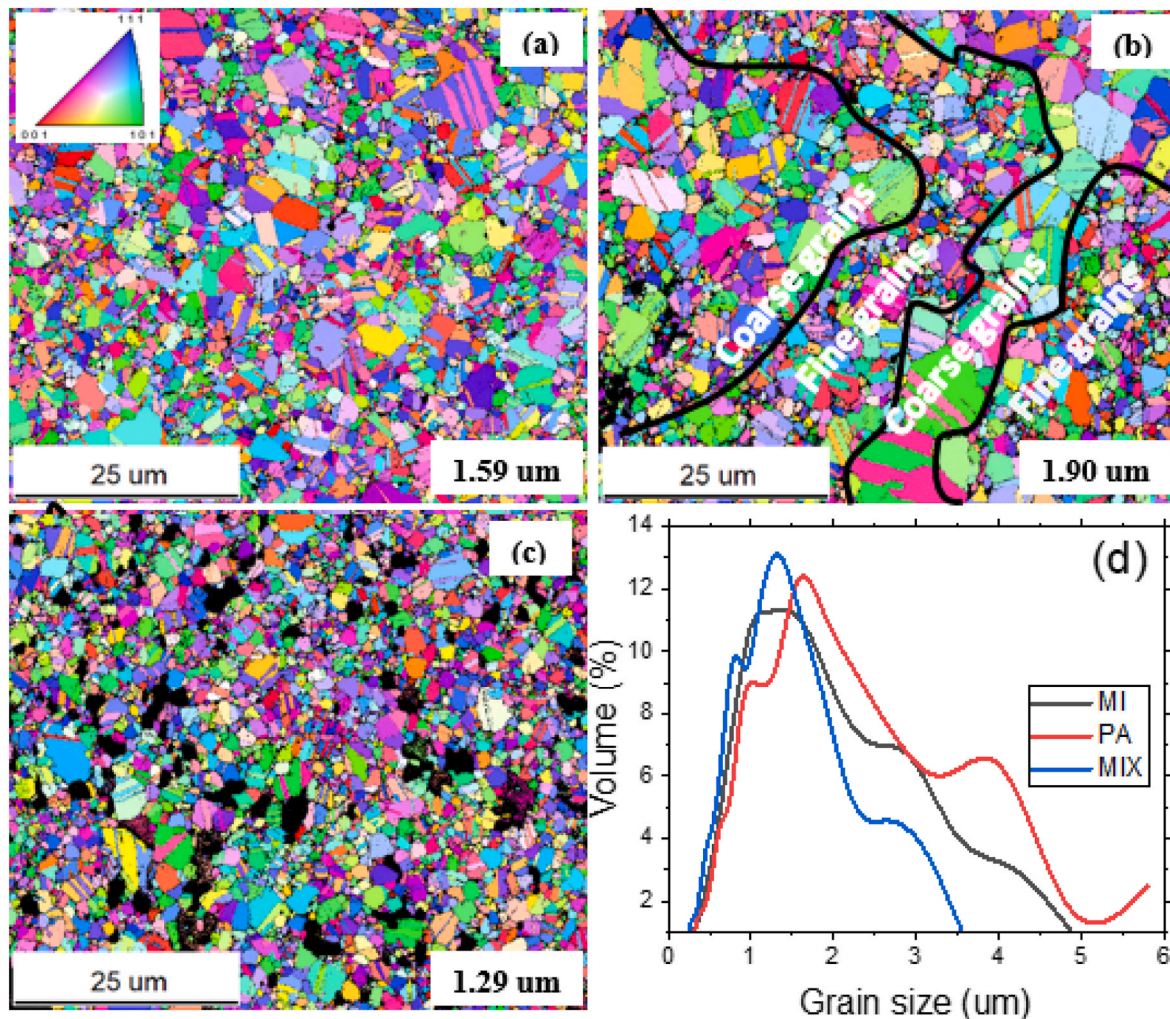


Fig. 7. EBSD orientation maps of (a) MI, (b) PA, and (c) MIX 1050 °C annealed samples; (d) Grain size distribution curves of MI, PA, and MIX samples.

(b). The trends of nanohardness as a function of annealing temperature are similar to those obtained using microhardness tests. This observation suggests no scale dependence. Generally, the difference between micro- and nanoscale does not exceed 10 %. The drop in nanohardness as a function of annealing temperature for all samples is evident; however, in the range between room temperature and 850 °C, the average nanohardness value of MIX is maintained, which confirms the microhardness measurements. On the other hand, the nanohardness trend of the PA sample might be described with robust agreement using a descending line trend (red line in Fig. 10 (b)). Notably, a trend in the microhardness of PA indicates that the hardness loss up to 850 °C is almost negligible (see Table 5).

Because a maximal load of 50 mN was used, the nanoindentation tests allowed us to first evaluate the heterogeneity of the materials. Recorded data with the indent observation by SEM revealed two different nanohardness ranges reflecting the matrix phase and coarse particles or agglomerates of precipitates. The nanohardness of the coarse particles is much higher ( $\gg 10$  GPa) than that of the agglomerates of precipitates (5–7 GPa). The nanohardness of precipitate agglomerates reflects both precipitates and the matrix below the particles. This relation can be observed in Fig. 10(c and d).

Despite the most uniform microstructure, the MIX sample annealed at 1050 °C presents the highest nanohardness standard deviation of the annealed samples. The opposite effect was observed during the microhardness test. As mentioned before, the random distribution of precipitates made it challenging to distinguish a signal from the matrix and

precipitates visible on the cross-section or present slightly below it. Given that the results of nanohardness in individual indents strongly depend on the presence of a hard secondary phase, all results were treated as the hardness of the matrix phase. This approach leads to an increase in the standard deviation. However, it allows one to consider a much higher number of indents. In the case of the microhardness test, the penetration depth of the indenter caused the deformation of a much larger volume of the material. Consequently, the number of precipitates deformed each time by the indenter is comparable, and the hardness values measured at each point are similar. This observation may also explain the visible difference between the micro- and nanohardness of the 850 °C as-annealed PA sample.

#### 4. Discussion

This paper examines the evolution of the microstructure and mechanical properties of CoCrFeNi high-entropy alloys produced using Mechanical Alloying with low BPR and the Spark Plasma Sintering technique. The preparation process of the consolidated samples was differed by one characteristic milling parameter. The impact of high milling speed, milling intervals, and pre-milling of selected elements with the lowest diffusion coefficients was studied. Moreover, a comprehensive assessment of all the analyzed influential factors was used to prepare the fourth sample. A benchmark sample was also prepared to check if manufacturing using similar parameters but with a higher BPR is possible. The measured densities of the samples are

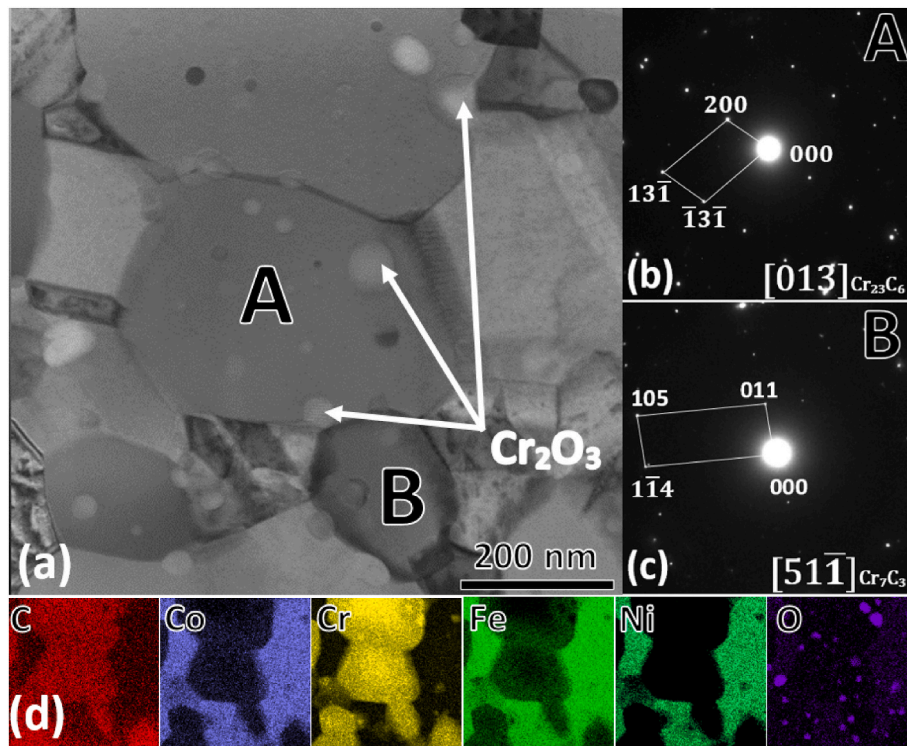


**Fig. 8.** (a) TEM bright field image of as-sintered MIX sample with marked regions A and B, (b) SAD pattern of region A, (c) SAD pattern of region B, (d) EDS analysis of Fig. 8 (a) region.

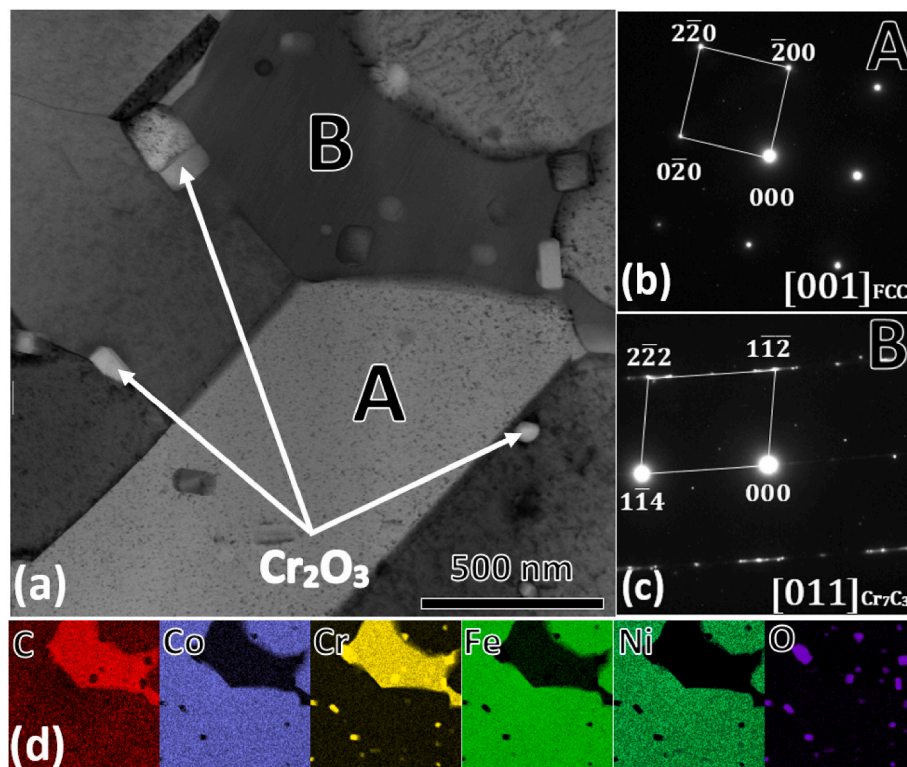


**Fig. 9.** (a) TEM bright field image of as-annealed 1050 °C MIX sample with marked regions A and B, (b) SAD pattern of region A, (c) SAD pattern of region B, (d) EDS analysis of Fig. 9 (a) region.

collected in Table 1. The results show a high densification level of all samples, which was then amplified by the heat treatment process. The XRD patterns of the bulk materials presented in Figs. 2 and 3 show the

formation of a single FCC phase with carbide reinforcement structures. Different carbides were formed depending on the process. Table 3 shows that the carbides in the MIX sample have a much higher volume than in

**Table 4**  
Secondary phases in different samples.

Sample	Process	Cr <sub>23</sub> C <sub>6</sub>	Cr <sub>7</sub> C <sub>3</sub>	Cr <sub>2</sub> O <sub>3</sub>
BM	Sintered	+	-	+
	Annealed 1050 °C	+	+	+
MS	Sintered	+	-	+
	Annealed 1050 °C	+	-	+
MI	Sintered	+	-	+
	Annealed 1050 °C	+	-	+
PA	Sintered	+	-	+
	Annealed 850 °C	+	-	+
MIX	Annealed 1050 °C	+	+	+
	Sintered	+	+	+
	Annealed 850 °C	+	-	+
	Annealed 1050 °C	-	+	+

**Table 5**  
Microhardness test results.

Hardness [HV1]	BM	MS	MI	PA	MIX
Sintered	361 ± 14	343 ± 19	368 ± 20	383 ± 9	409 ± 16
Annealed 850 °C	-	-	-	378 ± 14	386 ± 15
Annealed 1050 °C	288 ± 9	263 ± 25	283 ± 9	297 ± 9	315 ± 5

the other samples. Microstructure observations from the sintered samples presented in Fig. 4 have revealed the evolution of the strengthening phase by implementing the pre-alloying process and then with further process improvement in the MIX sample. The samples milled in one milling cycle present coarse strengthening particles surrounded by a

ring. In contrast, after an extra milling process, fine precipitates forming agglomerates and then evenly distributed structures after process optimization were observed. The annealing process results in matrix and particle homogenization, as shown in Fig. 6. The TEM analysis convinced us to name ‘light grey’ precipitates as Cr<sub>23</sub>C<sub>6</sub> and ‘dark grey’ precipitates as Cr<sub>7</sub>C<sub>3</sub>, which was demonstrated in Figs. 8 and 9. Moreover, a significant mechanical property improvement was observed after implementing the pre-alloying process. Compared to the one milling cycle processes, the microhardness increased by 11 %. Notably, the high micro/nanohardness stability of a MIX sample in a wide temperature range is also demonstrated in Table 5 and Fig. 10.

4.1. Microstructure evolution

The literature data show that Chromium atom incorporation in the matrix phase is the biggest obstacle in manufacturing FCC high entropy alloys via powder metallurgy techniques, especially using low ball-to-powder ratio. Chromium always tends to form phases with hardly-controlled composition, including the Cr-rich phase [10], Chromium oxides [41], σ phase [42], or other intermetallic structures [11] instead of forming a single FCC crystal structure. On the other hand, the presence of Chromium is strongly desirable due to the functional property improvement [43,44]. Our results show that bulk sintered samples synthesized through the one-step milling process with low BPR present too low efficiency to overcome this issue during the assumed milling time. The XRD patterns of mechanically alloyed powders presented in Fig. 1 indicated that the modification of one milling parameter does not help in reaching the scope of obtaining a homogeneous single-phase

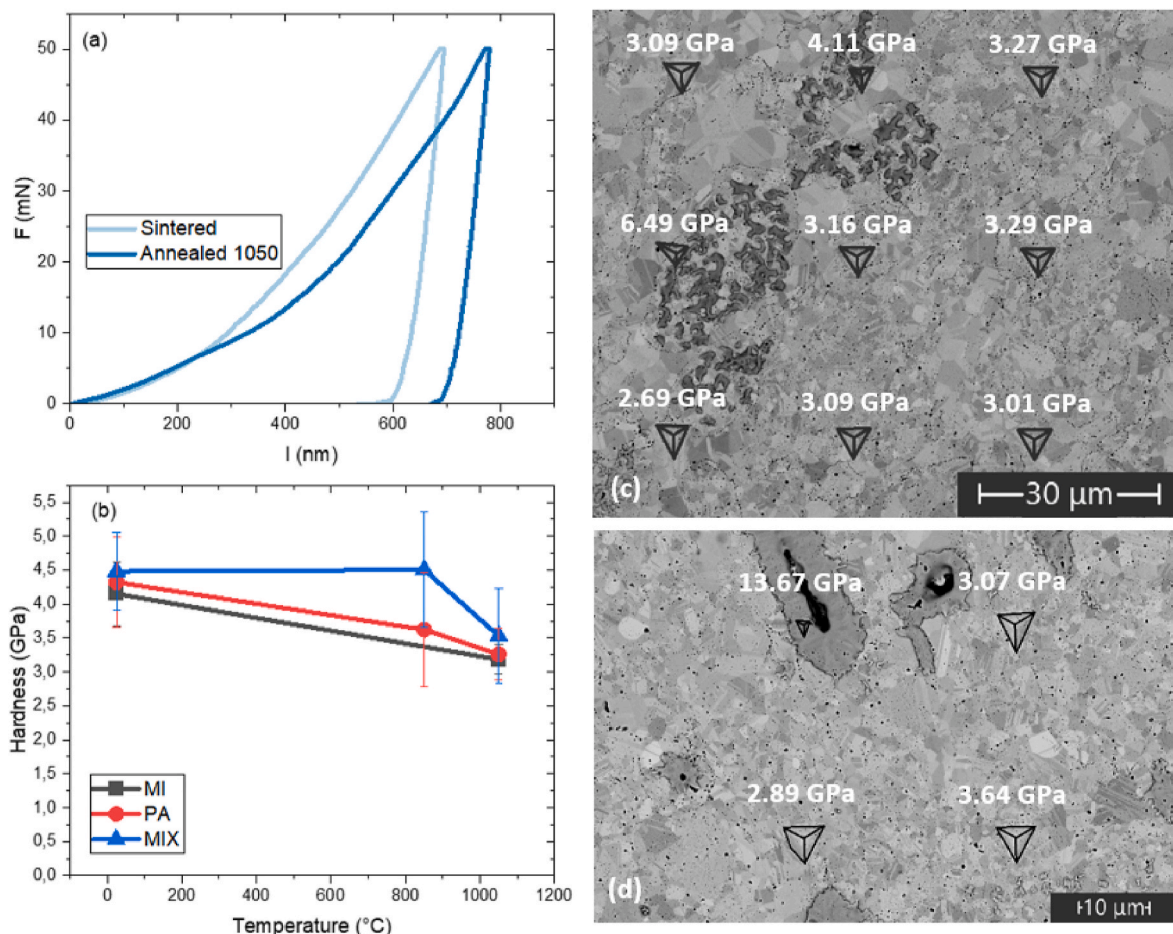


**Fig. 10.** (a) L-D curves recorded for MIX sample after sintering and annealing at 1050 °C; (b) nanohardness results of MI, PA, and MIX as a function of annealing temperature; SEM images with marked indents of 1050 °C PA (c) and 1050 °C MI (d).

precursor powder. After sintering, the formation of the dominant FCC crystal structure with common lattice parameter (3.57 Å) was observed. However, EDS analysis in Fig. 4 (c) revealed some Ni-, Co- and Fe enrichment areas that indicate slight but visible segregation of primary elements. The presence of almost pure Chromium particles confirms that the mechanical alloying process's efficiency might still be further improved. The largest Chromium particles unreacted during the MA remain in a sintered sample matrix. Both different crystal structures and the highest melting point among the selected primary elements did not allow them to mix with other elements and form a single phase in consequence. Surprisingly, the effects of Chromium in the X-ray diffraction patterns were not observed. This observation proved that the amount of the Cr-rich phase is below the detection level of the XRD technique. Comparing quantitative phase analysis results with the results already published by our group [21], where minor effects of Cr were observed, it is justified to claim that recorded homogenization was forced by the milling parameters optimization, but the results are still unsatisfactory. At this moment, it is worth noting that the Chromium particles are surrounded by shells. The XRD patterns revealed that some  $\text{Cr}_{23}\text{C}_6$  was formed during the sintering process. Because chromium carbides were not detected in the powder materials, we suppose that carbides tend to develop during the sintering process. We believe carbide formation is related to using the organic solvent  $\text{C}_7\text{H}_{18}$  as a process control agent. The carbon atoms bond with chromium due to their high affinity associated with the number of valence electron configurations during heat and current implementation [13]. The heat treatment process induces a higher diffusion rate, which induces further carbon migration through the midpoint of a particle. This effect results in the disappearance of Chromium particles and the formation of  $\text{M}_{23}\text{C}_6$  over the entire particle volume. The amount of Carbon was probably too low to cover the whole particle, so some chromium atoms migrated through the matrix phase, which increased Cr in the matrix-annealed samples. The other potential reasons of chromium carbides formation are tungsten carbide jar and balls utilized in a milling process or the graphite die usage during the sintering process. However, we believe that the strongest effect comes from the organic solvent. All the problems described above were not overcome even after higher BPR employment.

As a consequence of pre-alloying process implementation in PA, an evident difference was detected from the above results. The large and hard Chromium powder particles finally began to crumble, causing Cr–Ni-rich areas. EDS and TEM data of sintered samples revealed the formation of chromium carbide agglomerates inside the Cr–Ni-rich regions. Recorded maps strongly suggest the impact of the pre-milling process on the formation of the secondary phase. The higher efficiency of the Cr–Ni alloying process facilitates carbide nucleation during the sintering process. The low efficiency of the main milling process results in the agglomerates remaining. Worth noting is the significantly smaller grain size in areas with Cr–Ni-rich saturation. Lower energy delivered in the main milling process prevents the fragmentation of Cr–Ni particles, resulting in Cr–Ni-rich regions with Cr–C inside the particles. The annealing process caused the homogenization of a matrix phase and promoted a stable  $\text{Cr}_{23}\text{C}_6$ . Higher temperature annealing caused the dual carbide structure and bimodal grain size distribution.

In turn, the milling efficiency increment during the manufacturing of the MIX sample, and an evident FCC peak change in milled powders was observed. This suggests that more atoms migrate to the main phase, resulting in high structural deformation. Compared with the microstructural observation of the PA sample, the number of Cr–Ni regions was limited. The elevated efficiency of the milling process facilitates the fragmentation of all particles, forces the formation of a single FCC phase, and eases the uniform distribution of chromium particles. Consequently, carbide particles formed during sintering are evenly distributed in the sample volume. The dual carbide structure found in this sample might be related to the rapid sintering process and the local chemical anomaly, like Co-rich areas, which stabilize  $\text{Cr}_7\text{C}_3$  instead of  $\text{Cr}_{23}\text{C}_6$ . The annealing process at a lower temperature caused a stabilization of  $\text{Cr}_{23}\text{C}_6$ ,

visible as light grey particles however, a higher temperature annealing process stabilized  $\text{Cr}_7\text{C}_3$ , known before as dark grey particles. Interestingly, forming a single FCC phase was possible even after the sintering process despite a very low BPR.

Some previous works [45,46] confirmed that at  $\sim 650^\circ\text{C}$ , the  $\text{Cr}_7\text{C}_3 > \text{Cr}_{23}\text{C}_6$  transformation for other materials was observed. This analysis confirmed the structural transformation (or stabilization) of  $\text{M}_{23}\text{C}_6$  after annealing. Surprisingly, annealing at higher temperatures of the BM, PA, and MIX samples promotes recombination, and the diffraction peaks of  $\text{Cr}_7\text{C}_3$  were detected. This observation strongly suggests that the efficiency of the milling process and the promotion of fine Cr precipitates after the milling process are responsible for this effect. Wang et al. [47] found that prolonged high-temperature annealing caused fine  $\text{M}_{23}\text{C}_6$  carbides to transform into  $\text{M}_7\text{C}_3$  in a Cr cast Iron alloy during the cooling process. A similar effect might be observed in the MIX sample. Two other samples also present the  $\text{Cr}_{23}\text{C}_6$  phase. This effect corresponds to the coarser particles found in both. The local amount of Carbon might be too low to promote  $\text{Cr}_7\text{C}_3$ . This observation might explain the lack of  $\text{Cr}_7\text{C}_3$  peaks in the as-annealed MI and MS samples.

#### 4.2. Functional property improvement

Depending on the chosen manufacturing process parameters, different strengthening effects occur. For the as-sintered MI, MS, and BM, unreacted Cr-rich particles with a shell of chromium carbides evenly distributed in a matrix are observed. The presence of a hard secondary phase results in a hardness increase. Our previous work revealed that chromium dissolution resulted in a hardness increase of a matrix phase [21]. Some literature data also show that the Cr implementation increases the hardness [35,43,44]. These results indicate that the Chromium dissolution results in mechanical property improvement. Further heat treatment processes caused the homogenization of the samples, and no Co-, Fe-, and Ni-rich areas were detected. Hardness loss after the annealing process was observed, however, a relatively low drop confirms the high stability of the materials. The presence of hard chromium carbides hinders grain growth during heat treatment. The hardness of the secondary phase reaches 15 GPa. This observation again confirms the close  $\text{Cr}_{23}\text{C}_6$  structure formation. Hirota et al. revealed that  $\text{Cr}_{23}\text{C}_6$  consolidated at a similar temperature presents a similar hardness (13.7–15 GPa) [48].

Implementing a two-step milling process in the PA sample results in Chromium carbide nucleation in Cr–Ni particles. The presence of Chromium carbide agglomerates caused a hardness increase in comparison with the one-milling-cycle samples. When annealed at  $850^\circ\text{C}$ , the sample demonstrates a slight hardness decrease. Notably, the average microhardness value is higher than the nanohardness, which is seldom observed. Although the difference does not exceed 10%, the uneven grain growth related to chromium carbide agglomeration is supposed to determine the difference in nanohardness in specified regions. The chromium carbide segregation facilitates uneven grain growth in areas where a lower number of Cr–C agglomerates are detected. Chromium carbide-depleted areas are more susceptible to the grain size increase effect. According to the Hall-Petch rule, the hardness increment of materials strongly depends on the average grain size reduction. Higher temperature annealing results in a further decrease in hardness.

The employment of a two-step, highly efficient milling process caused almost complete crushing of the agglomerates and led to an even distribution of chromium carbides in the matrix phase. This effect leads to a hardness increase. The observation made on the sample after lower temperature annealing confirms the high stability of the mechanical properties. Evenly distributed hard  $\text{Cr}_{23}\text{C}_6$  inhibits the local grain growth and stabilizes the mechanical properties. A slight microhardness decrease might be within the statistical error. A higher temperature again promotes the carbide transformation and hardness drop. As mentioned, high-temperature annealing with subsequent water

quenching constrains the  $\text{Cr}_{23}\text{C}_6 > \text{Cr}_7\text{C}_3$  transformation. This type of carbide phase plus grain size increase results in a hardness decrease. However, the hardness values measured at two scales still exceeded the hardness of the samples milled in one milling cycle.

In Table 6, the comparison of the microhardness of the MIX sample with other HEAs manufactured via powder metallurgy is summarized. The analysis of the results leads to the conclusion that the manufactured material presents similar hardness to the materials prepared using higher BPR. The higher BPR increases the probability of ball-powder contact, resulting in quicker synthesis and powder particle refinement. This effect promotes the average grain size reduction. According to the Hall-Petch rule, a slight difference might result from grain size refinement. Notably, the results presented in this paper clearly show that the mechanical properties of synthesized materials might be improved without increasing the ball-to-powder ratio. In situ, carbide formation in the sintered samples may increase temperature stability, while the annealing temperature allowed us to set an expected strength vs. ductility trade-off.

#### 4.3. Strategy for synthesis using a low BPR

The consideration presented above led us to the conclusion that the low BPR implementation does not act as a barrier to high-entropy alloys manufacturing. It is only through the process optimization that we observed a single FCC phase as a matrix formation with some reinforcing phases typically noticed before, when higher BPR was selected []. Moreover, the higher BPR utilized for BM sample manufacturing does not allow the all atoms incorporation through the matrix phase. This confirms that the BPR is a crucial, but not the most important parameter for mechanical-alloying process.

Comparing the obtained results with our previous work [21], one may assume that the presence of Cr-rich particles is the biggest challenge for low BPR manufacturing of an FCC high entropy alloy with Chromium. The energy delivered during milling was insufficient to crush the powder particles. Moreover, material prepared by a similar method with a higher BPR did not present a significant difference from a microstructural or functional point of view. The results show that the evolution of one milling parameter did not result in considerable process improvement, and a similar material might be prepared with a low BPR. Chromium particles with the highest melting point, low diffusion coefficient, and largest particle size promote the formation of coarse  $\text{M}_{23}\text{C}_6$  particles instead of the distribution of Cr atoms in the matrix phase.

The efficiency improvement might take place through the employment of a two-step milling process. A short pre-milling process caused greater Cr and Ni particle refinement and determined the preliminary alloying effect of elements with the lowest diffusion coefficient and the highest average particle size. Implementing higher BPR in the pre-alloying process is justified because a lower amount of initial powder was milled in this process (in total  $\% \text{Cr} + \% \text{Ni} \sim 50\%$ ). By adding Fe and Co after the pre-milling process, further crushing of the Cr–Ni rich phase and promoting of a single phase occurs. Furthermore, the improvement of the efficiency of the process results in a random distribution of Chromium carbides in a single FCC matrix phase.

An effective way to modify the properties of manufactured materials is to choose a proper annealing condition. Selecting a temperature to obtain the desired properties and hinder grain growth is necessary. It is visible that the presence of carbides in the lower temperature annealed sample caused the micro- and nanohardness to be maintained, whereas the higher temperature promotes the carbide transformation.

## 5. Conclusions

In summary, the impact of different process parameters on the microstructure evolution and mechanical properties of CoCrFeNi manufactured by low BPR MA + SPS was investigated. This paper proposes the two-step milling process as an efficient and more productive

**Table 6**  
Hardness comparison of obtained results with literature data.

Material	Process	BPR	Microhardness [HV]	Ref.
CoCrFeNi	MA + SPS	5:1	409 ± 16	This work
CoCrFeNi	MA + SPS	10:1	490 ± 10	[42]
CoCrFeMnNi	MA + SPS	10:1	400 ± 10	[49]
CoCrFeMnNi	MA + HIP	15:1	332	[50]
CoCrFeMnNi	MA + SPS	10:1	450 ± 10	[51]
$\text{Ni}_{1.5}\text{Co}_{1.5}\text{CrFeTi}_{0.5}$	MA + SPS	10:1	442	[41]
$\text{Fe}_{35}\text{Mn}_{10}\text{Cr}_{20}\text{Ni}_{35}$	MA + SPS	15:1	416	[52]

manufacturing path for high entropy alloys after sintering.

1. The manufactured samples presents the high densification level – even over 97 % of the theoretical density The density is reduced not only be pores, which number in annealed samples is limited, but also by different secondary phases formation.
2. The presented results confirm the insufficient efficiency of the one-step milling process using a low BPR. Coarse Cr-rich particles surrounded by a shell are forming instead of chromium atoms incorporation in a matrix phase. The rest of the elements are distributed randomly.
3. Implementing two-step mechanical alloying induces the formation of a Cr–Ni-rich phase with the nucleation of chromium carbides after sintering. Chromium carbides form clusters and cause bimodal grain size distribution as a consequence.
4. The optimization of the milling process efficiency elicits the refinement of Cr–Ni particles and promotes the random distribution of chromium carbides. The number of chromium carbide clusters was reduced significantly. Moreover, different heat treatment processes led to different carbide formations. Both types of carbides,  $\text{Cr}_{23}\text{C}_6$  and  $\text{Cr}_7\text{C}_3$ , were detected in sintered samples. The annealing process at 850 °C caused the evolution of  $\text{Cr}_7\text{C}_3$ , and only  $\text{Cr}_{23}\text{C}_6$  was found. The heat treatment process at 1050 °C presents a reverse trend, and only  $\text{Cr}_7\text{C}_3$  carbides were formed.
5. Chromium particle refinement during mechanical alloying caused the formation of fine carbide precipitates in sintered samples. Fine and uniformly distributed particles result in grain size decrease and hardness increase in consequence. Moreover, the same trends of micro- and nanohardness were observed, providing the mechanical properties stability in both scales.
6. Forming a single FCC phase with carbides and oxides reinforcement using low BPR with similar properties to samples manufactured with higher BPR is possible. Whenever the optimization procedure of mechanical alloying needs to be employed, the chemical composition must be regarded.

#### Declaration of competing interest

The authors declare that they have no known competing financial interests or personal relationships that could have appeared to influence the work reported in this paper.

#### Acknowledgements

We acknowledge support from the European Union Horizon 2020 research and innovation program under NOMATEN Teaming grant (agreement no. 857470) and from the European Regional Development Fund via the Foundation for Polish Science International Research Agenda PLUS program grant No. MAB PLUS/2018/8. The publication was created within the framework of the project of the Minister of Science and Higher Education "Support for the activities of Centres of Excellence established in Poland under Horizon 2020" under contract no. MEiN/2023/DIR/3795.

## Appendix A. Supplementary data

Supplementary data to this article can be found online at <https://doi.org/10.1016/j.jmrt.2024.03.116>.

## References

- [1] Kumar A, Singh A, Suhane A. Mechanically alloyed high entropy alloys: existing challenges and opportunities. *J Mater Res Technol* 2022;17:2431–56. <https://doi.org/10.1016/j.jmrt.2022.01.141>.
- [2] Murty BS, Yeh JW, Ranganathan S. Synthesis and processing. *High Entropy Alloy* 2014;77–89. <https://doi.org/10.1016/b978-0-12-800251-3.00005-5>.
- [3] Chen R, Zheng S, Zhou R, Wei B, Yang G, Chen P, et al. Development of cemented carbides with CoCrFeNiCu high-entropy alloy binder prepared by spark plasma sintering. *Int J Refract Met Hard Mater* 2022;103. <https://doi.org/10.1016/j.ijrmhm.2021.105751>.
- [4] Peng S, Lu Z, Yu L. Effects of Y2O3/Ti/Zr addition on microstructure and hardness of ODS-CoCrFeNi HEAs produced by mechanical alloying and spark plasma sintering. *J Alloys Compd* 2021;861. <https://doi.org/10.1016/j.jallcom.2020.157940>.
- [5] Liu L, Han T, Cao SC, Liu Y, Shu J, Zheng C, et al. Enhanced wearing resistance of carbide reinforced FeCoNiCrMn high entropy alloy prepared by mechanical alloying and spark plasma sintering. *Mater Today Commun* 2022;30:103127. <https://doi.org/10.1016/j.mtcomm.2022.103127>.
- [6] Gwalani B, Pohan RM, Waseem OA, Alam T, Hong SH, Ryu HJ, et al. Strengthening of Al0.3CoCrFeMnNi-based ODS high entropy alloys with incremental changes in the concentration of Y2O3. *Scripta Mater* 2019;162:477–81. <https://doi.org/10.1016/j.scriptamat.2018.12.021>.
- [7] Li M, Guo Y, Wang H, Shan J, Chang Y. Microstructures and mechanical properties of oxide dispersion strengthened CoCrFeNi high-entropy alloy produced by mechanical alloying and spark plasma sintering. *Intermetallics* 2020;123:106819. <https://doi.org/10.1016/j.intermet.2020.106819>.
- [8] Zhang Y, Zuo TT, Tang Z, Gao MC, Dahmen KA, Liaw PK, et al. Microstructures and properties of high-entropy alloys. *Prog Mater Sci* 2014;61:1–93. <https://doi.org/10.1016/j.pmatsci.2013.10.001>.
- [9] Javdan M, Reihanian M, Gheisari K. Mechanically alloyed (FeCoNi)75Cu25–xSix high entropy alloys: phase evaluation and magnetic properties. *J Alloys Compd* 2023;952. <https://doi.org/10.1016/j.jallcom.2023.170030>.
- [10] Akhlaghi P, Amirjan M, Parvin N. The effect of processing parameters and heat-treatment on the microstructure and mechanical properties of PM CoCrFeMnNiTi0.1 high-entropy alloy. *Mater Chem Phys* 2021;257:123722. <https://doi.org/10.1016/j.matchemphys.2020.123722>.
- [11] Alcalá MD, Real C, Fombella I, Trigo I, Córdoba JM. Effects of milling time, sintering temperature, Al content on the chemical nature, microhardness and microstructure of mechanochemically synthesized FeCoNiCrMn high entropy alloy. *J Alloys Compd* 2018;749:834–43. <https://doi.org/10.1016/j.jallcom.2018.03.358>.
- [12] Huang M, Jiang J, Wang Y, Liu Y, Zhang Y. Effects of milling process parameters and PCAs on the synthesis of Al0.8Co0.5Cr1.5CuFeNi high entropy alloy powder by mechanical alloying. *Mater Des* 2022;217:110637. <https://doi.org/10.1016/j.matdes.2022.110637>.
- [13] Ruiz-Esparza-Rodríguez MA, Garay-Reyes CG, Estrada-Guel I, Hernández-Rivera JL, Cruz-Rivera JJ, Gutiérrez-Castañeda E, et al. Influence of process control agent and Al concentration on synthesis and phase stability of a mechanically alloyed AlxCoCrFeMnNi high-entropy alloy. *J Alloys Compd* 2021;882:160770. <https://doi.org/10.1016/j.jallcom.2021.160770>.
- [14] Sriharitha R, Murty BS, Kottada RS. Alloying, thermal stability and strengthening in spark plasma sintered AlxCoCrCuFeNi high entropy alloys. *J Alloys Compd* 2014;583:419–26. <https://doi.org/10.1016/j.jallcom.2013.08.176>.
- [15] Laurent-Brocq M, Goujon P-A, Monnier J, Villeroy B, Perriere L, Pires R, et al. Microstructure and mechanical properties of a CoCrFeMnNi high entropy alloy processed by milling and spark plasma sintering. *J Alloys Compd* 2019;780:856–65. <https://doi.org/10.1016/j.jallcom.2018.11.181>.
- [16] Vaidya M, Anupam A, Bharadwaj JV, Srivastava C, Murty BS. Grain growth kinetics in CoCrFeNi and CoCrFeMnNi high entropy alloys processed by spark plasma sintering. *J Alloys Compd* 2019;791:1114–21. <https://doi.org/10.1016/j.jallcom.2019.03.341>.
- [17] Yeh JW. Alloy design strategies and future trends in high-entropy alloys. *Jom* 2013;65:1759–71. <https://doi.org/10.1007/s11837-013-0761-6>.
- [18] Kelly JP, Graeve OA. Spark plasma sintering as an approach to manufacture bulk materials: Feasibility and cost savings. *Jom* 2015;67:29–33. <https://doi.org/10.1007/s11837-014-1202-x>.
- [19] Cavaliere P. Spark plasma sintering of materials: Advances in processing and applications. 2019. <https://doi.org/10.1007/978-3-030-05327-7>.
- [20] Miracle DB, Senkov ON. A critical review of high entropy alloys and related concepts. *Acta Mater* 2017;122:448–511. <https://doi.org/10.1016/j.actamat.2016.08.081>.
- [21] Olejarz A, Huo WY, Zieliński M, Diduszko R, Wyszowska E, Kosińska A, et al. Microstructure and mechanical properties of mechanically-alloyed CoCrFeNi high-entropy alloys using low ball-to-powder ratio. *J Alloys Compd* 2023;938. <https://doi.org/10.1016/j.jallcom.2022.168196>.
- [22] Průša F, Šenková A, Kučera V, Capek J, Vojtěch D. Properties of a high-strength ultrafine-grained CoCrFeNiMn high-entropy alloy prepared by short-term mechanical alloying and spark plasma sintering. *Mater Sci Eng A* 2018;734:341–52. <https://doi.org/10.1016/j.msea.2018.08.014>.
- [23] Moravcik I, Cizek J, Gavendova P, Sheikh S, Guo S, Dlouhy I. Effect of heat treatment on microstructure and mechanical properties of spark plasma sintered AlCoCrFeNiTi0.5 high entropy alloy. *Mater Lett* 2016;174:53–6. <https://doi.org/10.1016/j.matlet.2016.03.077>.
- [24] Salemi F, Abbasi MH, Karimzadeh F. Synthesis and thermodynamic analysis of nanostructured CuNiCoZnAl high entropy alloy produced by mechanical alloying. *J Alloys Compd* 2016;685:278–86. <https://doi.org/10.1016/j.jallcom.2016.05.274>.
- [25] Suprianto Chen CL. Study of (Ni,Cr) pre-milling for synthesis of CoFe(NiCr)Mn high entropy alloy by mechanical alloying. *Mater Sci Eng A* 2021;807:140810. <https://doi.org/10.1016/j.msea.2021.140810>.
- [26] Zhang Z, Wang Q, Mu D, Shen G, Liu M, Zhang M, et al. Microstructure evolution and mechanical properties of CoCrFeNiAl0.3 high entropy alloy produced by ball milling in combination with thermomechanical consolidation. *Mater Char* 2022;187:111833. <https://doi.org/10.1016/j.matchar.2022.111833>.
- [27] Colombini E, Rosa R, Trombi L, Zadra M, Casagrande A, Veronesi P. High entropy alloys obtained by field assisted powder metallurgy route: SPS and microwave heating. *Mater Chem Phys* 2018;210:78–86. <https://doi.org/10.1016/j.matchemphys.2017.06.065>.
- [28] Gates-Rector S, Blanton T. The Powder Diffraction File: a quality materials characterization database. *Powder Diffr* 2019;34:352–60. <https://doi.org/10.1017/S0885715619000812>.
- [29] Rietveld HM. Line profiles of neutron powder-diffraction peaks for structure refinement. *Acta Crystallogr* 1967;22:151–2. <https://doi.org/10.1107/S0365110X67000234>.
- [30] Rietveld HM. A profile refinement method for nuclear and magnetic structures. *J Appl Crystallogr* 1969;2:65–71. <https://doi.org/10.1107/S0021889869006558>.
- [31] Balzar D. X-ray diffraction line broadening: modeling and applications to high-Tc superconductors. *J Res Natl Inst Stand Technol* 1993;98:321. <https://doi.org/10.6028/jres.098.026>.
- [32] Stephens PW. Phenomenological model of anisotropic peak broadening in powder diffraction. *J Appl Crystallogr* 1999;32:281–9. <https://doi.org/10.1107/S0021889898006001>.
- [33] Leineweber A. Understanding anisotropic microstrain broadening in Rietveld refinement. *Z Krist* 2011;226:905–23. <https://doi.org/10.1524/zkri.2011.1413>.
- [34] Zhang R, Zhao S, Ding J, Chong Y, Jia T, Ophus C, et al. Short-range order and its impact on the CrCoNi medium-entropy alloy. *Nature* 2020;581:283–7. <https://doi.org/10.1038/s41586-020-2275-z>.
- [35] Praveen S, Murty BS, Kottada RS. Phase evolution and densification behavior of nanocrystalline multicomponent high entropy alloys during spark plasma sintering. *Jom* 2013;65:1797–804. <https://doi.org/10.1007/s11837-013-0759-0>.
- [36] Warren BE. X-ray diffraction. Addison-Wesley Publishing Company Inc.; 1969.
- [37] Mckay F, Ismael T, Robinson A, Kizilkaya O, Sprunger PT, Derosa PA. Surface oxidation mechanism of CoCrFeNi high entropy alloy. *Surf Sci* 2022;122124. <https://doi.org/10.1016/j.susc.2022.122124>.
- [38] Dahlborg U, Cornide J, Calvo-Dahlborg M, Hansen TC, Fitch A, Leong Z, et al. Structure of some CoCrFeNi and CoCrFeNiPd multicomponent HEA alloys by diffraction techniques. *J Alloys Compd* 2016;681:330–41. <https://doi.org/10.1016/j.jallcom.2016.04.248>.
- [39] Rogal L, Kalita D, Tarasek A, Bobrowski P, Czerwinski F. Effect of SiC nanoparticles on microstructure and mechanical properties of the CoCrFeMnNi high entropy alloy. *J Alloys Compd* 2017;708:344–52. <https://doi.org/10.1016/j.jallcom.2017.02.274>.
- [40] Zaborowska K, Kurpaska Wyszowska E, Azarov A, Turek M, Kosińska A, et al. High versus low energy ion irradiation impact on functional properties of PLD-grown alumina coatings. *Nucl Instruments Methods Phys Res Sect B Beam Interact with Mater Atoms* 2023;540:24–9. <https://doi.org/10.1016/j.nimb.2023.03.027>.
- [41] Moravcik I, Cizek J, Zapletal J, Kovacova Z, Vesely J, Minarik P, et al. Microstructure and mechanical properties of Ni1.5Co1.5CrFeTi0.5 high entropy alloy fabricated by mechanical alloying and spark plasma sintering. *Mater Des* 2017;119:141–50. <https://doi.org/10.1016/j.matdes.2017.01.036>.
- [42] Praveen S, Murty BS, Kottada RS. Alloying behavior in multi-component AlCoCrCuFe and NiCoCrCuFe high entropy alloys. *Mater Sci Eng A* 2012;534:83–9. <https://doi.org/10.1016/j.msea.2011.11.044>.
- [43] Xu J, Kong X, Chen M, Wang Q, Wang F. High-entropy FeNiCoCr alloys with improved mechanical and tribological properties by tailoring composition and controlling oxidation. *J Mater Sci Technol* 2021;82:207–13. <https://doi.org/10.1016/j.jmst.2020.12.042>.
- [44] Yan X, Guo H, Yang W, Pang SJ, Wang Q, Liu Y, et al. Al0.3CrxFeCoNi high-entropy alloys with high corrosion resistance and good mechanical properties. *J Alloys Compd* 2021;860:158436. <https://doi.org/10.1016/j.jallcom.2020.158436>.
- [45] Wierzchzak K, Bala P, Dziurka R, Tokarski T, Cios G, Koziel T, et al. The effect of temperature on the evolution of eutectic carbides and M7C3 → M23C6 carbides reaction in the rapidly solidified Fe-Cr alloy. *J Alloys Compd* 2017;698:673–84. <https://doi.org/10.1016/j.jallcom.2016.12.252>.
- [46] Cui H, Tao K, Zhou X, Zhang J. Thermal stability of nanostructured NiCrC coating prepared by HVAF spraying of cryomilled powders. *Rare Met* 2008;27:418–24. [https://doi.org/10.1016/S1001-0521\(08\)60155-2](https://doi.org/10.1016/S1001-0521(08)60155-2).
- [47] Wang J, Li C, Liu H, Yang H, Shen B, Gao S, et al. The precipitation and transformation of secondary carbides in a high chromium cast iron. *Mater Char* 2006;56:73–8. <https://doi.org/10.1016/j.matchar.2005.10.002>.
- [48] Hirota K, Mitani K, Yoshinaka M, Yamaguchi O. Simultaneous synthesis and consolidation of chromium carbides (Cr3C2, Cr7C3 and Cr23C6) by pulsed electric-

- current pressure sintering. *Mater Sci Eng A* 2005;399:154–60. <https://doi.org/10.1016/j.msea.2005.02.062>.
- [49] Nagarjuna C, Song JW, Jeong KY, Pin MW, Song G, Lee JK, et al. Developing harmonic structure in CoCrFeMnNi high entropy alloy to enhance mechanical properties via powder metallurgy approach. *J Mater Res Technol* 2022;17:1686–95. <https://doi.org/10.1016/j.jmrt.2022.01.098>.
- [50] Cheng H, Chen W, Liu X, Tang Q, Xie Y, Dai P. Effect of Ti and C additions on the microstructure and mechanical properties of the FeCoCrNiMn high-entropy alloy. *Mater Sci Eng A* 2018;719:192–8. <https://doi.org/10.1016/j.msea.2018.02.040>.
- [51] Nagarjuna C, Yong Jeong K, Lee Y, Min Woo S, Ig Hong S, Seop Kim H, et al. Strengthening the mechanical properties and wear resistance of CoCrFeMnNi high entropy alloy fabricated by powder metallurgy. *Adv Powder Technol* 2022;33:103519. <https://doi.org/10.1016/j.apt.2022.103519>.
- [52] Zhou J, Liao H, Chen H, Huang A. Carbon-alloyed Fe<sub>35</sub>Mn<sub>10</sub>Cr<sub>20</sub>Ni<sub>35</sub> high entropy alloy synthesized by mechanical alloying plus spark plasma sintering. *J Alloys Compd* 2021;859:157851. <https://doi.org/10.1016/j.jallcom.2020.157851>.